Modeling and simulation of a heat source in electric arc welding

Isabelle Choquet[1], Håkan Nilsson[2], Margarita Sass-Tisovskaya[1]
[1]University West, Department of Engineering Science, Trollhättan, Sweden,
[2]Chalmers University of Technology, Department of Applied Mechanics, Gothenburg, Sweden
isabelle.choquet@hv.se

ABSTRACT

This study focused on the modeling and simulation of a plasma heat source applied to electric arc welding. The heat source was modeled in three space dimensions coupling thermal fluid mechanics with electromagnetism. Two approaches were considered for calculating the magnetic field: i) three-dimensional, and ii) axi-symmetric. The anode and cathode were treated as boundary conditions. The model was implemented in the open source CFD software OpenFOAM-1.6.x. The electromagnetic part of the solver was tested against analytic solution for an infinite electric rod. Perfect agreement was obtained. The complete solver was tested against experimental measurements for Gas Tungsten Arc Welding (GTAW) with an axi-symmetric configuration. The shielding gas was argon with thermodynamic and transport properties covering a temperature range from 200 to 30 000 K. The numerical solutions then depend greatly on the approach used for calculating the magnetic field. The axi-symmetric approach indeed neglects the radial current density component, mainly resulting in a poor estimation of the arc velocity. Various boundary conditions were set on the anode and cathode. These conditions, difficult to measure and to estimate a priori, significantly affect the plasma heat source simulation results. Solution of the temperature and electromagnetic fields in the electrodes will thus be included in the forthcoming developments.

Keywords: electric arc welding, electric heat source, thermal plasma, magnetic potential, spatial distribution of thermal energy, TIG, GTAW, WIG.

1 INTRODUCTION

Electric welding as a method of assembling metal parts through fusion is an old technology. This manufacturing process is however still under intensive development, in order to further improve different aspects such as process productivity, process control, and weld quality. Such improvements are beneficial both from economical and environmental sustainability.

The electric arc welding process is interdisciplinary in nature, and complex to master as it involves very large temperature gradients and a number of parameters that do interact in a non-linear way. Its investigation was long based on experimental studies. Today, thanks to recent and significant progress done in the field of welding simulation, experiments can be complemented with numerical modeling to reach a deeper process understanding. As an illustration, the change in microstructure can be simulated for a given thermal history, as in [1]. The numerical calculation of the residual stresses, to investigate fatigue and distortion, can now be coupled with the weld pool as in [2], calibrating functional approximations of volume and surface heat flux transferred from the electric arc.

Electric arcs used in welding are generally formed coupling an electric discharge between anode and cathode with a gas flow. A main goal is to form a shielding gas flow characterized by temperatures large enough to melt the materials to be welded, i.e.

a thermal plasma flow. The numerical modeling of a thermal plasma flow is thus a base element for characterising the thermal history of an electric welding process, by calculating the thermal energy provided to the work-piece, and its spatial distribution.

A thermal plasma is basically modeled coupling thermal fluid mechanics (governing mass, momentum and energy or enthalpy) with electromagnetism (governing the electric field, the magnetic field, and the current density). Different versions of this model can be found in the literature in the context of electric arc welding simulation. They were developed to address in more detail various aspects of electric arc welding heat source. As an illustration, a simulation model for axi-symmetric configurations, describing consistently the arc core, sheath, and the solid electrodes was developed in [3], and applied to Gas Tungsten Arc Welding (GTAW). Other models account for thermal non-equilibrium [4], or for the influence of metal vapour on the thermodynamic and transport properties of a plasma arc [5]. Coupled arc and weld pool simulation tools were recently developed within the frame of axi-symmetric configurations [6], without considering the plasma sheath (that is the transition layer between arc and electrode, and between arc and parent metal). At least one of these tools also account for 3-dimensional effects and arc dynamic behavior [7].

The modeling and simulation of an electric arc heat source within the frame of welding started only recently in Sweden. The rigorous derivation of a fluid arc model from kinetic theory was done in [8]. The development of a simulation tool for calculating the heat source was initiated in [9]. The present study, in the continuation of [9], focuses on the plasma arc heat source, to calculate quantities such as the thermal energy provided by an electric arc, and its three-dimensional spatial distribution. Such data could be used as input for predicting via simulation weld pool behavior, as well as the thermal history of the base metal (for example within the heat affected zone).

The thermal plasma model is described in section 2. It couples a simplified system of Maxwell equations (section 2.1) with a system of thermal Navier-Stokes equations in three space-dimensions (section 2.2). The anode and cathode are treated as boundary conditions. Two approaches are considered for calculating the magnetic field: i) three-dimensional, and ii) axi-symmetric, as detailed in section 2.1. The model was implemented in the open source software OpenFOAM 1.6.x (www.openfoam.com). The electromagnetic part of the solver was tested against analytic solution for an infinite electric rod. The test case and the results are presented in section 3.1. The complete solver was tested against experimental measurements for GTAW. The configuration was axi-symmetric, and the shielding gas was argon. This second test case, and the related simulation results, are presented in section 3.2. For each test case both approaches for calculating the magnetic field were used, and the validity of the simplified (or axi-symmetric) version discussed. The influence of the boundary conditions (set on the electrodes) on the arc temperature and velocity were investigated. The main results and conclusions are summarised in section 4.

2 MODEL

An electric welding arc heat source is modeled here in three space dimensions coupling thermal fluid mechanics with electromagnetism. The fluid and electromagnetic models are tightly coupled. The Lorentz force, or magnetic pinch force, resulting from the induced magnetic field indeed acts as the main cause of plasma flow acceleration. The Joule heating because of the electric field is the largest heat source governing the plasma energy (and thus temperature). On the other hand the system of equations governing electromagnetism is temperature dependent, via the electric conductivity. The main specificities of the implemented electromagnetic and thermal fluid model are as follow.

2.1 Electromagnetic model

The electromagnetic component of the model is derived from the Maxwell equations (see [9] for further derivation details), assuming:
- a Debye length λ_D much smaller than the characteristic length of the welding arc, thus local electro-neutrality in the plasma core,
- characteristic time and length of the welding arc allowing neglecting the convection current compared to the conduction current in Ampere's law, resulting in quasi-steady electromagnetic phenomena,
- a Larmor frequency much smaller than the average collision frequency of electrons, implying a negligible Hall current compared to the conduction current, and

- a magnetic Reynolds number much smaller than unity, leading to a negligible induction current compared to the conduction current.
Then, the electric potential V is governed by the Laplace equation,

$$\nabla \cdot [\sigma(T)\ \nabla V] = 0\ , \tag{1}$$

where T is the temperature, ∇ denotes the gradient operator, and $\nabla\cdot$ the divergence operator. The electric conductivity $\sigma(T)$ is temperature dependent, as illustrated in Fig.1 for an argon plasma.

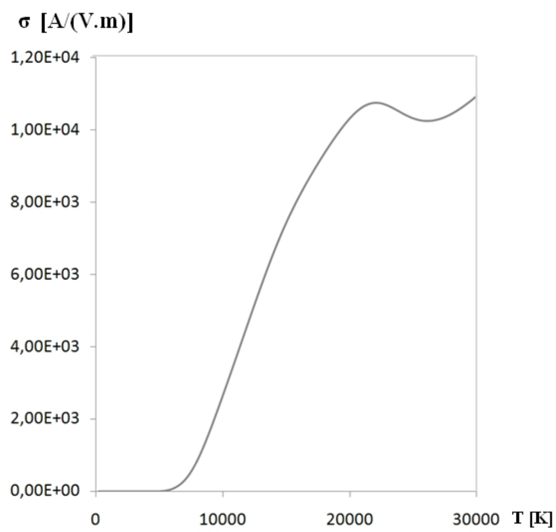

Figure 1: Argon plasma electric conductivity as function of temperature.

The electric field $\vec{E}$, is defined from the gradient of the electric potential,

$$\vec{E} = -\nabla V\ . \tag{2}$$

The electric current density $\vec{J}$ is given by Ohm's law,

$$\vec{J} = -\sigma(T)\ \nabla V\ . \tag{3}$$

Two approaches are used in this paper for calculating the magnetic field, $\vec{B}$. One of them computes the magnetic potential field $\vec{A}$ in 3-space dimensions, Eq. (4), and from that the magnetic field, Eq. (5). While the other, called axi-symmetric approach, computes only one component of the magnetic field, Eq. (6).

The magnetic potential $\vec{A}$ is governed by the Poisson equation,

$$\triangle \vec{A} = \sigma(T)\ \mu_o\ \nabla V\ , \tag{4}$$

where $\triangle$ denotes the Laplace operator, and μ_o the permeability of free space. The magnetic field $\vec{B}$ is defined in 3-space dimensions as the rotational of the magnetic potential,

$$\vec{B} = \nabla \times \vec{A}\ , \tag{5}$$

where $\nabla\times$ denotes the rotational operator.
For axi-symmetric configurations the calculation of the magnetic field, Eqs. (4)-(5), is often reduced to the single angular component

$$B_\theta(r) = \frac{\mu_o}{r} \int_0^r J_{axial}(l)\ l\ dl\ , \tag{6}$$

where r is the radial distance to the symmetry axis, and J_{axial} the axial component of the current density. Notice that this simplified expression is obtained doing an additional assumption sometimes omitted: the current density vector is axial, that is aligned with the direction of the symmetry axis. So axi-symmetric configurations should also be invariant by translation along the symmetry axis to satisfy this additional condition.

2.2 Fluid model

The thermal fluid component of the model applies to a Newtonian and thermally expansible fluid, assuming:
- a one-fluid model,
- in local thermal equilibrium, and
- mechanically incompressible, because of the small Mach number.

The model is thus suited to the plasma core. The treatment of the plasma sheath would require a two-fluid model with partial thermal equilibrium, to account for electron diffusion, and for the temperature difference observed in the sheath between electrons and heavy particles.
In the present framework, and with steady-state conditions, the continuity equation is written as

$$\nabla \cdot [\rho(T)\ \vec{u}] = 0\ , \tag{7}$$

where ρ denotes the fluid density, and $\vec{u}$ the fluid velocity. The density $\rho(T)$ is here temperature dependent, as illustrated for argon plasma in Fig. 2.

The momentum conservation equation is expressed as

$$\begin{aligned}&\nabla\cdot\left[\,\rho(T)\;\vec{u}\otimes\vec{u}\right]-\vec{u}\;\nabla\cdot\left[\rho(T)\;\vec{u}\right]\\&\quad-\nabla\cdot\left[\mu(T)\;\left(\nabla\vec{u}+(\nabla\vec{u})^{T}\right)-\tfrac{2}{3}\;\mu(T)\;(\nabla\cdot\vec{u})I\right]\\&\quad=-\nabla P+\vec{J}\times\vec{B}\;,\end{aligned}\tag{8}$$

where the operators $\otimes$ and $\times$ denote the tensorial and vectorial product, respectively. I is the identity tensor, μ the viscosity, and P the pressure. The last term on the right hand side of Eq. (8) is the Lorentz force.

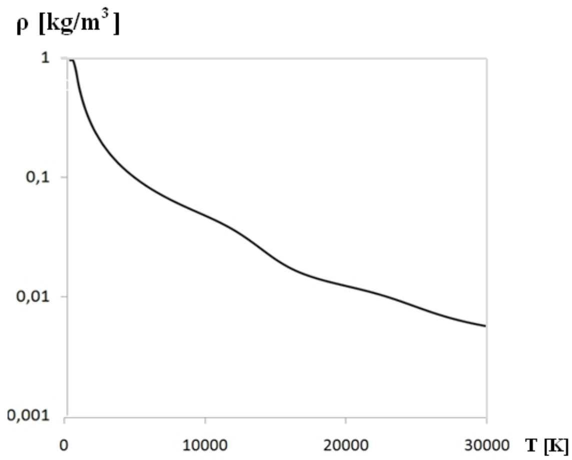

Figure 2: Argon plasma density as function of temperature.

The enthalpy conservation equation is

$$\begin{aligned}&\nabla\cdot\left[\rho(T)\vec{u}\;\;h\right]-h\;\nabla\cdot\left[\rho(T)\;\vec{u}\right]-\nabla\cdot\left[\alpha(T)\;\nabla h\right]\\&\quad=\nabla\cdot(\vec{u}\;P)-P\;\nabla\cdot\vec{u}+\vec{J}\cdot\vec{E}\\&\quad-Q_{rad}+\nabla\cdot\left[\frac{5\;k_B\;\vec{J}}{2\;e\;C_p(T)}\;h\right],\end{aligned}\tag{9}$$

where h is the specific enthalpy, α is the thermal diffusivity, Q_{rad} the radiation heat loss, k_B the Boltzmann constant, e the elementary charge, and C_p the specific heat at constant pressure. The third term on the right hand side of Eq. (9) is the Joule heating, and the last term the transport of electron enthalpy. The temperature, T, is derived from the specific enthalpy via the definition of the specific heat:

$$C_p(T)=\left(\frac{dh}{dT}\right)_P\tag{10}$$

The thermodynamic and transport properties (derived in [10] using kinetic theory) were implemented in the form of data tables for a temperature range from 200 to 30 000 K.

3 TEST CASES

Two test cases were considered. The first one, an infinite rod, was retained since it has an analytic solution allowing testing the electromagnetic part of the simulation model, and the two calulation methods for the magnetic field. The second is the water cooled GTAW test case described in [11]. It was investigated experimentally in [12], and used in the literature as reference case for testing arc heat source simulation models.

3.1 Infinite rod

The magnetic field induced in and around an infinite rod of radius r_o with constant electric conductivity, and constant current density parallel to the rod axis, reduces to an angular component B_θ with the following analytic expression (see [9] for further details):

$$\begin{aligned}B_\theta(r)&=\frac{\mu_o J_{axial} r}{2}\quad if\quad r<r_o\;,\\B_\theta(r)&=\frac{\mu_o J_{axial} r_o^2}{2\;r}\quad if\quad r\geq r_o\;.\end{aligned}\tag{11}$$

$J_{axial}=I/(\pi\;r_o)$ denotes the current density along the rod axis, and I the current intensity.

A long rod of radius $r_o = 1$ mm with the large and uniform electric conductivity $\sigma_{rod} = 2700A/(Vm)$, surrounded by a poor conducting region of radius $r_{ext} = 16$ mm, and uniform electric conductivity $\sigma_{sur} = 10^{-5}A/(Vm)$, was simulated. Notice that the conductivity σ_{rod} and σ_{sur} correspond to an argon plasma at 10600 and 300 K, respectively.

The electric potential difference applied on the rod was set to 707 V, as indicated in Fig. 3. It corresponds here to a current intensity of 600 A. The electric potential gradient along the direction normal to the boundary was set to zero on all the other boundaries.

The magnetic field was calculated using both the i) three-dimensional approach, Eqs. (4)-(5), and the ii) axi-symmetric approach, Eq. (6). In the three-dimensional approach, the magnetic potential $\vec{A}$ was set to zero at $r = r_{ext}$, and its gradient along the direction normal to the boundary was set to zero on all the other boundaries.

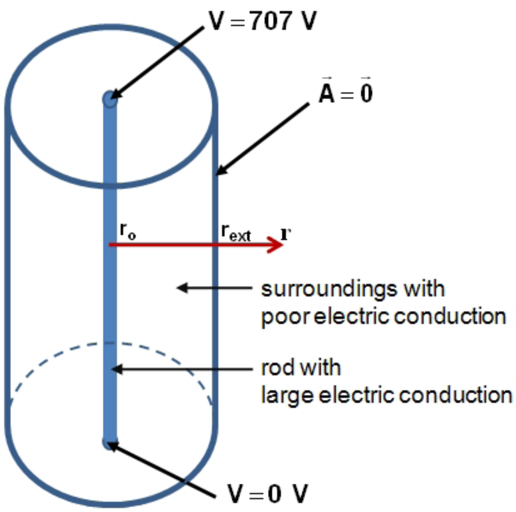

Figure 3: Schematic representation of the computational domain.

The calculation results, plotted in Fig. 4 for the angular component of the magnetic field, are both in perfect agreement with the analytic solution, as expected when the current density is aligned with the symmetry axis.

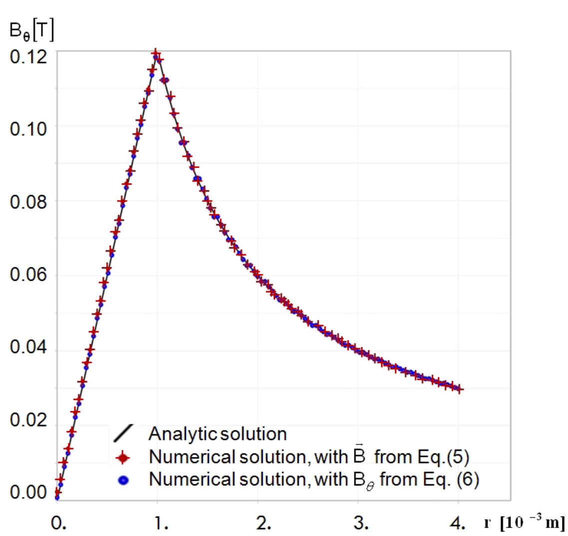

Figure 4: Angular component of the magnetic field along the radial direction ($r_o = 1 \times 10^{-3}$m).

3.2 Water cooled GTAW

The 2 mm long and 200 A argon arc studied in [11], based on the experimental measurements of [12] reported in Fig. 5, is now considered.

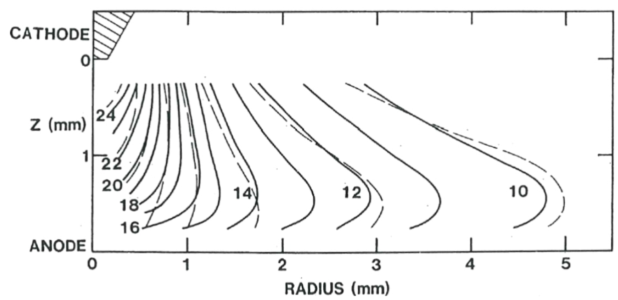

Figure 5: Temperature measurements of [12].

The configuration is sketched Fig. 6. The electrode, of radius 1.6 mm, has a conical tip of angle 60° truncated at a tip radius of 0.5 mm. The electrode is mounted inside a ceramic nozzle of internal and external radius 5 mm and 8.2 mm, respecively. The pure argon shielding gas enters the nozzle at room temperature and at an average mass flow rate of $1.66 \cdot 10^{-4}$ m^3/s.

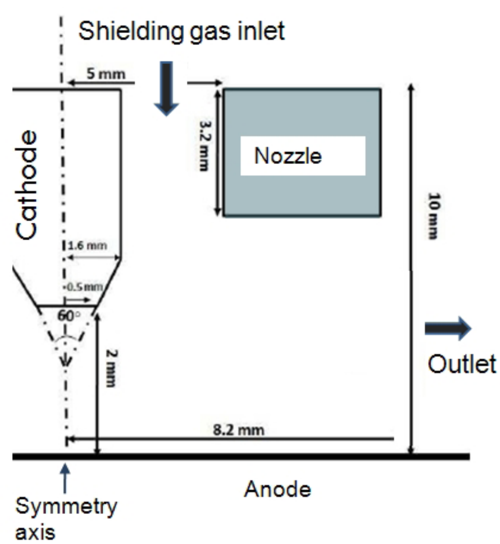

Figure 6: Schematic representation of the GTAW test case

The temperature and the current density set on the cathode boundary are explicitely given in [11]. The anode surface temperature was also set as proposed in [11], extrapolating the experimental results of [12]. Looking at the experimental results, Fig. 5, it can be noticed that the measured temperature is rather difficult to extrapolate up to the anode. The boundary conditions set on the cathode also suffer from a lack of accuracy, as experimental measurements cannot be done in the very close vicinity of the electrodes. These difficulties may explain the variety of boundary conditions used in the literature for simulating this test case.

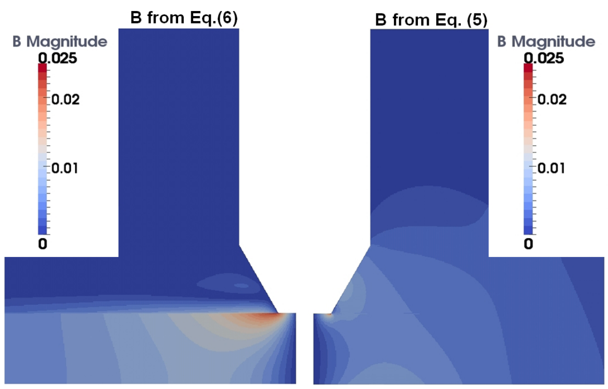

Figure 7: Magnetic field magnitude calculated with the axi-symmetric (left) and the three-dimensional (right) $\vec{B}$-approach.

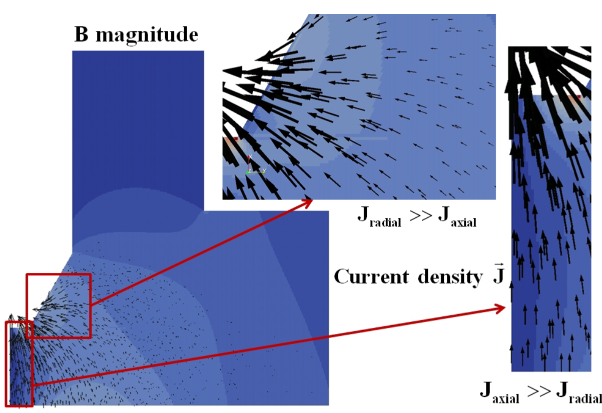

Figure 8: Current density vector calculated with the three-dimensional approach, Eqs (4)-(5) .

The magnetic field was calculated using both the i) three-dimensional approach, Eqs. (4)-(5), and the ii) axi-symmetric approach, Eq (6). The axi-symmetric approach is simpler, and often used in the literature to simulate GTAW problems. The numerical results from the two approaches significantly differ, as shown in Fig. 7. Agreement is only observed below the cathode tip, where the non-axial component of the current density is negligible compared to the axial component (see Fig. 8). The axi-symmetric approach indeed neglects the radial current density component. The three-dimensional calculation, Fig. 8, shows that the non-axial component of the current density is not everywhere negligible, in particular next to the electrode tip, where the largest induced magnetic field is observed. Neglecting the non-axial component of the current density would first of all result in a poor estimation of the magnetic pinch forces, and in turn of the arc velocity, as well as the pressure force the arc exerts on the work piece. Consequently, the axi-symmetric approach was not retained for simulating this axi-symmetric GTAW configuration.

The next simulation results were all obtained with the three-dimensional approach, Eqs (4)-(5).

The calculated temperature is plotted along the symmetry axis in Fig. 9, and along the radial direction 1 mm above the anode in Fig. 10. In a similar way, the calculated velocity is plotted along the symmetry axis in Fig. 11, and along the radial direction 1 mm above the anode in Fig. 12.

The simulation results plotted for the so-called coarse (resp. fine) mesh were calculated using 25 (resp. 100) uniform cells along the 0.5 mm tip radius, and 100 (resp. 200) uniform cells between the electrodes along the symmetry axis. It can be observed that the quality of the mesh first affects the amplitute of the temperature decrease just below the electrode tip (see Fig. 9), and the maximum velocity reached between cathode tip and anode (see Fig. 11).

The experimental data available in [12] and shown Fig. 5 are used for comparison with the numerical results along the radial direction, in Fig. 10. A good agreement is obtained.

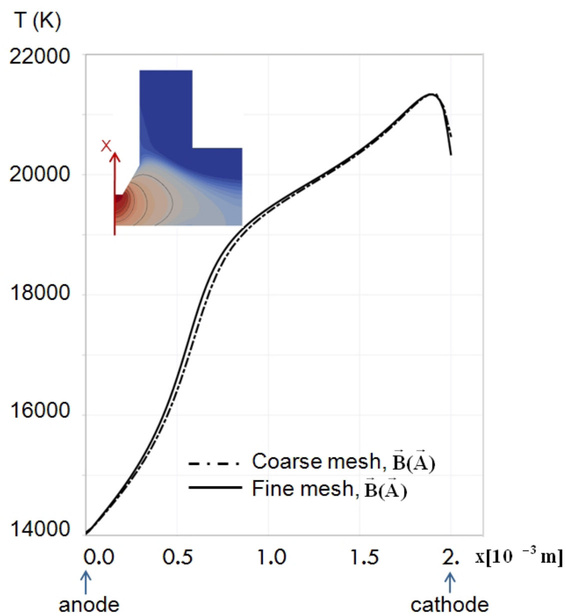

Figure 9: Temperature along the symmetry axis.

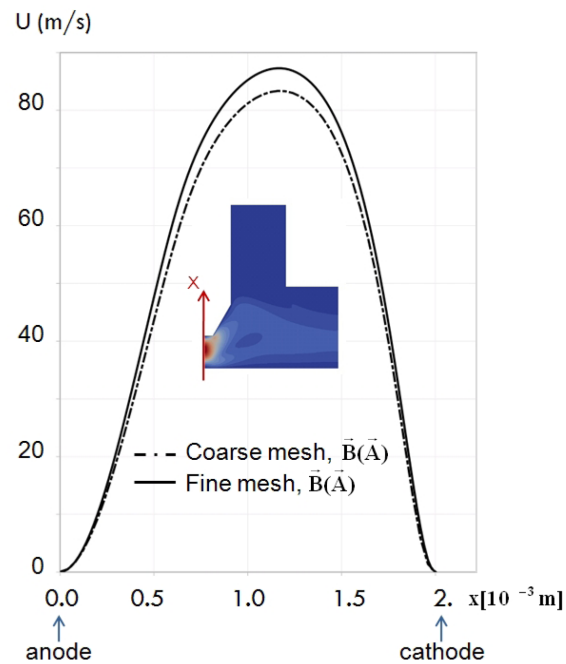

Figure 11: Velocity along the symmetry axis.

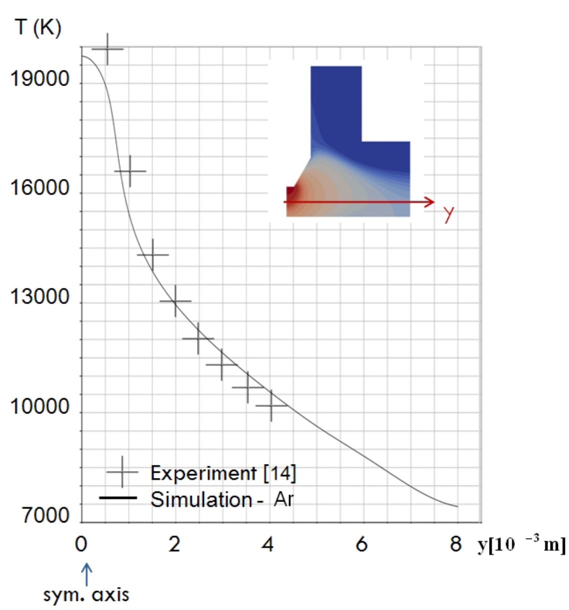

Figure 10: Temperature along the radial direction, 1 mm above the anode.

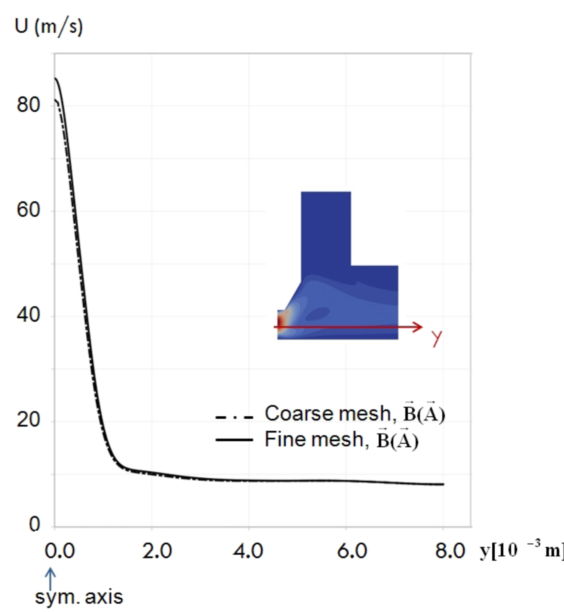

Figure 12: Velocity along the radial direction, 1 mm above the anode.

The comparison along the symmetry axis is difficult to perform, as the isotherms represented in Fig. 6 are not plotted in this area. We can however observe that the maximum temperature obtained numerically seems to underestimate the experimental one by about 10%. This could be due to the boundary conditions set on the electrodes. Other conditions also used in the literature are now considered.

Three cases, denoted a, b and c, are compared in Fig. 13 to 15. In case a (treated above using the boundary conditions defined in [11]), the current density is uniform on the 0.5 mm radius cathode tip, and it decreases linearly down to zero as the radius tip increases. In case b all the current density (also uniform) goes through the 0.5 mm radius cathode tip. The boundary conditions on the anode are the same in case a and b. In case c the boundary conditions on the cathode are the same as in case b. Case c is associated with an extreme thermal condition on the anode for testing the model: its anode does not conduct heat.

The three test cases were simulated using the same mesh, with 25 cells along the 0.5 mm tip radius, and 100 cells between the electrodes along the symmetry axis.

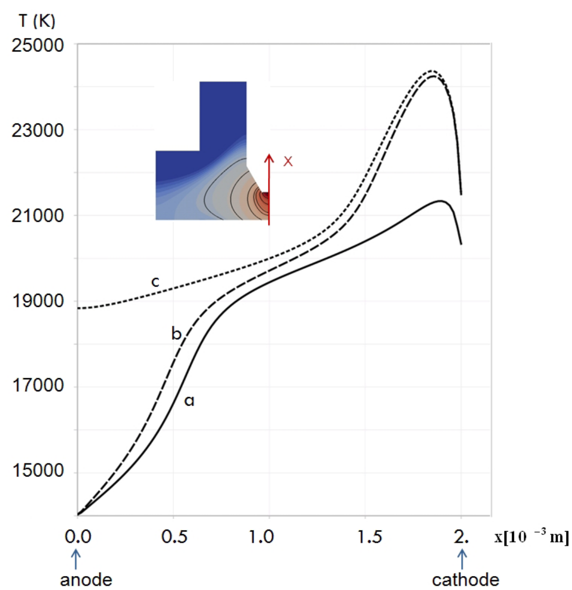

Figure 13: Influence of the electrode boundary conditions on the temperature along the symmetry axis.

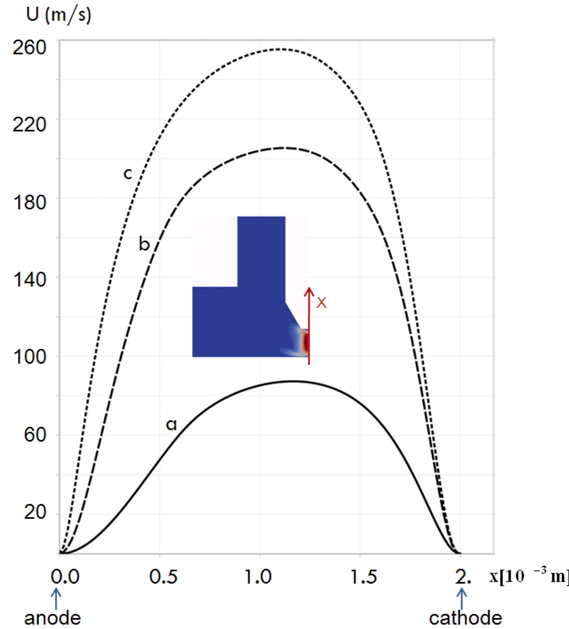

Figure 14: Influence of the electrode boundary conditions on the velocity along the symmetry axis.

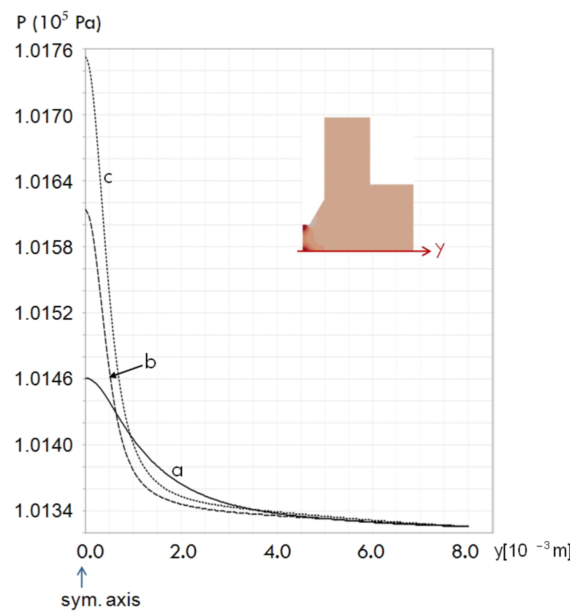

Figure 15: Influence of the electrode boundary conditions on the pressure on the base metal.

The temperature calculated for each case is plotted along the symmetry axis in Fig. 13, while the velocity is plotted in Fig. 14. It can be observed in Fig. 13 that the current density distribution on the cathode has a large influence on the maximum arc temperature. Also, compared to case a, the maximum temperature of case b is much closer to the maximum temperature observed experimentaly. The thermal boundary condition on the anode has almost no influence on the maximum arc temperature. However, it can significantly affect the heat transferred to the base metal, as it changes significantly the temperature close to the anode.
Finally, Figs. 14 and 15 show that the velocity along the symmetry axis, and the pressure force on the work piece, are significantly changed for each variation tested on the electrode boundary conditions.

4 CONCLUSION

This study focused on the modeling and simulation of an electric arc heat source in three space dimensions, coupling thermal fluid mechanics with electromagnetism. The model was implemented in the open source software OpenFOAM 1.6.x. Two approaches were considered for calculating the magnetic field $\vec{B}$: i) three-dimensional, and ii) axi-symmetric.
The electromagnetic part of the solver was tested against analytic solution for an infinite electric rod. The solutions are in perfect agreement.
The complete solver was tested against experimental measurements for GTAW with an axi-symmetric configuration, and argon as shielding gas. The numerical solutions for the $\vec{B}$-field then significantly differ. The axi-symmetric approach indeed neglects the radial current density component. For axi-symmetric configurations that are not invariant by translation along the symmetry axis, such as GTAW, this simplification is not everywhere justified. Consequently, the axi-symmetric approach, Eq. (6), was not retained for simulating the GTAW heat source. The numerical results obtained using the three-dimensional approach, Eqs. (4)-(5), show a good agreement with the available experimental results.
However, various boundary conditions can be set on the electrodes, as these conditions are difficult to measure and to estimate a priori. In addition they significantly affect the simulation results. Temperature and current density distribution on the electrode surfaces should thus be calculated rather than set, to enhance the predictive capability of the simulation model. Solution of the temperature and electromagnetic fields in the electrodes will thus be included in the forthcoming development of the simulation model.

Acknowledgment: The authors thank Prof. Jacques Aubreton and Prof. Marie-Françoise Elchinger for the data tables of thermodynamic and transport properties they did provide. This work was supported by KK-foundation in collaboration with ESAB, Volvo Construction Equipment and SSAB. Håkan Nilsson was in this work financed by the Sustainable Production Initiative and the Production Area of Advance at Chalmers. These supports are gratefully acknowledged.

5 References

[1] Lindgren, L., B. Babu, C. Charles, and D. Wedberg (2010). Simulation of manufacturing chains and use of coupled microstructure and constitutive models. *Finite Plasticity and Visco-plasticity of Conventional and Emerging Materials*, Khan, A. S. and B. Farrokh, (red.). NEAT PRESS, 4 s.

[2] Kumar, A. and T. DebRoy (2007). Heat transfer and fluid flow during Gas-Metal-Arc fillet welding for various joint configurations and welding positions. *The minerals, metals and materials society and ASM International*.

[3] Wendelstorf J. (2000). Ab initio modelling of thermal plasma gas discharges (electric arcs). PhD. Thesis, Carolo-Wilhelmina University, Germany.

[4] Tanaka, Y., T. Michishita and Y. Uesugi (2005). Hydrodynamic chemical non-equilibrium model of a pulsed arc discharge in dry air at atmospheric pressure. *Plasma Sources Sci. Technol.* **14**, pp. 134-151

[5] Yamamoto, K., M. Tanaka, S. Tashiro, K. Nakata, K. Yamazaki, E. Yamamoto, K. Suzuki, and A.B. Murphy (2008). Numerical simulation of metal vapor behavior in arc plasma. *Surface and Coatings Technology*, **202**, pp. 5302-5305.

[6] Hu, J. and L.S. Tsai (2007). Heat and mass transfer in gas metal arc welding. Part I: The arc, Part II: The metal. *International Journal of Heat and Mass Transfer* 50, pp. 808-820, 833-846.

[7] Xu, G., J. Hu and H.L. Tsai (2009). Three-dimensional modeling of arc plasma and metal transfer in gas metal arc welding. *International Journal of Heat and Mass Transfer*, **52**, pp. 1709-1724.

[8] Choquet, I. and B. Lucquin-Desreux (2011), Non equilibrium ionization in magnetized two-temperature thermal plasma, *Kinetic and Related Models*, **4**, to appear. Preprint: http://www.ljll.math.upmc.fr/publications/2010/R10043.php

[9] Sass-Tisovskaya, M. (2009). *Plasma arc welding simulation with OpenFOAM*, Licentiate Thesis, Chalmers University of Technology, Gothenburg, Sweden.

[10] Rat, V., A. Pascal, J. Aubreton, M.F. Elchinger, P. Fauchais and A. Lefort (2001). Transport ptoperties in a two-temperature plasma: theory and application. *Physical Review E*, **64**, 2.

[11] Tsai M.C and Sindo Kou (1990). Heat transfer and fluid flow in welding arcs produced by sharpened and flat electrodes. *Int J. Heta Mass Transfer*, **33**, 10, pp. 2089-2098.

[12] Haddad, G.N. and A.J.D. Farmer (1985) Temperature measurements in gas tungsten Arcs. *Welding Journal* **24**, pp. 339-342.